

Dual-type atomic Ru promoted bifunctional catalytic process realizing ultralow overpotential for Li-O₂ batteries

Yun Guo ^a, Peng Wang ^{a,d,*}, Yunjie Liu ^a, Shan Guo ^a, Lei Shi ^b, Jingrui Sun ^a, Yu Tian ^a, Xiaojun Wang ^a, Shenlong Zhao ^{b,**}, Zhiming Liu ^{a,c,*}

^a College of Electromechanical Engineering, Shandong Engineering Laboratory for Preparation and Application of High-Performance Carbon-Materials, Qingdao University of Science & Technology, Qingdao 266061, PR China

^b CAS Key Laboratory of Nanosystem and Hierarchical Fabrication, CAS Center for Excellence in Nanoscience, National Center for Nanoscience and Technology, Beijing, 100190, PR China

^c Qingdao Industrial Energy Storage Research Institute, Qingdao Institute of Bioenergy and Bioprocess Technology, Chinese Academy of Sciences, Qingdao 266101, PR China

^d Qingdao Key Laboratory of Functional Membrane Material and Membrane Technology, Qingdao Institute of Bioenergy and Bioprocess Technology, Chinese Academy of Sciences, Qingdao 266101, PR China



ARTICLE INFO

Keywords:
Li-O₂ battery
Cross-scale catalyst
Li₂O₂
ORR/OER
Kinetics

ABSTRACT

Developing well-defined catalysts to ameliorate overpotential and cycling capability is imperative for high-performance Li-O₂ batteries. However, conventional catalysts face fundamental challenges that ORR and OER with different rate-determining steps are catalyzed by the same active center, inevitably weakening the selectivity and activity. Herein, we report a cross-scale catalyst with ultrafine RuPt nanoparticles and surrounding RuPt pairs on porous carbon (RuPt NPs@RuPt-N-C). The planted Ru single atoms within Pt nanoparticles and carbon matrix contribute to a fresh bifunctional catalytic mechanism for enhancing ORR/OER catalytic kinetics. As a proof-of-concept application in Li-O₂ batteries, this catalyst realizes extremely low overpotentials of only 0.43 V and superior cyclic stability of 209 cycles at 200 mA g⁻¹. Experimental and computational results disclose that for Pt NPs@Pt-N-C without Ru functionalization, only Pt-N-C works as ORR/OER active centers. By contrast, for RuPt NPs@RuPt-N-C, due to downshifted d-band center and enhanced charge transfer with LiO₂ intermediate, the Pt nanocrystals are fully activated by Ru atoms, making RuPt nanocrystals as preferable ORR kinetics promoter for the formation of easily-decomposed nanoflower Li₂O₂. Moreover, adjacent RuPt pairs with weakened O₂ affinity can work as major OER center, contributing to accelerating the following Li₂O₂ decomposition. This work expands the frontier of cross-scale electrocatalysts with tailored bifunctional catalysis properties for other electrocatalytic fields.

1. Introduction

Aprotic lithium-oxygen (Li-O₂) batteries have been of great interest due to their high theoretical energy density (\approx 3500 Wh kg⁻¹, based on O₂+ 2Li⁺ + 2e⁻ \leftrightarrow Li₂O₂) far exceeding the benchmark of lithium-ion batteries. However, the formation and decomposition of the insulated discharge products (Li₂O₂) corresponding to the oxygen reduction reaction (ORR) and the oxygen evolution reaction (OER) respectively, always need to overcome high energy barrier and result in inferior overpotential [1–6]. As a consequence, the nucleation, growth and

decomposition chemistry at triple-phase boundary actually governs the overall electrochemical performance of Li-O₂ batteries. While, various cathode catalysts are of crucial importance in modulating the morphology, size, distribution and crystallinity of Li₂O₂ species on their surfaces, which are anticipated to induce the continuous generation of Li₂O₂ during ORR and rapid decomposition during OER [7–10].

In the past year, carbon-supported noble metal (Ru, Pd, Ir, Pt, etc) or their alloy catalysts still have been proven as the most competitive in Li-O₂ batteries field due to excellent charge transfer rate, high atom utilization efficiency and superior metal-support electronic interactions

* Corresponding authors at: College of Electromechanical Engineering, Shandong Engineering Laboratory for Preparation and Application of High-Performance Carbon-Materials, Qingdao University of Science & Technology, Qingdao 266061, PR China.

** Corresponding author.

E-mail addresses: pengwang@qust.edu.cn (P. Wang), zhaosl@nanoctr.cn (S. Zhao), zmliu@qust.edu.cn (Z. Liu).

[11–20]. Although the assembled form of metal atoms can be divided into single atom (SAs), nanoclusters (NCs) and nanoparticles (NPs) with different configurations, these carbon-supported catalysts commonly provide preferable catalysis platform for Li-O₂ batteries. However, these carbon-supported catalysts commonly possess monotone-scale metal active site with single coordination environment such as SAs-N-C, NCs-N-C or NPs-N-C. It is mentioned that ORR/OER processes in Li-O₂ batteries involve complex reversible conversion with multiple intermediates generated in multielectron processes. From an energetic perspective, the reversible ORR/OER processes of Li-O₂ batteries accompanied with various oxygen-contained intermediates adsorption/desorption ($O_2 \leftrightarrow LiO_2 \leftrightarrow Li_2O_2 \leftrightarrow Li_3O_4 \leftrightarrow Li_4O_4$) definitely demonstrate two different rate-determining steps (RDS). Hence, these carbon-supported catalysts with monotonous metal coordination environments may be efficient in driving a one-way reaction, but they are not the optimal sites to efficiently catalyze the reverse process at the same time. This is contradictory with the bifunctional catalytic kinetics and thus leaves enough room for further ameliorating the electrochemical performance of Li-O₂ batteries at atomic level.

In response, to balance the competition between ORR and OER at the same site, a class of new emerging cross-scale hybrids assembled by two or more scales of metal constituents (such as SAs, NCs or NPs) within an individual catalyst have been implemented in a variety of catalysis fields [21–27]. Compared with single-scale catalysts, the combination of SAs, NCs or NPs with multiple active sites has better catalytic selectivity and activity for specific reaction pathways. For instance, the Pt-based catalyst with dual active sites of Pt SAs and Pt₃Co NPs, exhibits preferable catalytic activity for acidic ORR [23]. Moreover, the synergistic effect between Ru single-atoms and nanoclusters was reported for their excellent catalytic activity to boost the kinetics in alkaline hydrogen evolution reaction [28]. The hybrid electrocatalyst containing Pt-Fe alloy nanoparticles and atomically dispersed Pt/Fe single atoms demonstrate synergistic effects in boosting the performance of proton exchange membrane fuel cells [29]. It is worth mentioning that there is almost no report about cross-scale catalysts for ORR/OER in Li-O₂ batteries and underlying mechanism investigations have been rarely concerned to date. In theory, cross-scale catalysts with electronic synergy between different active sites could provide more flexible absorption and desorption configurations for various intermediates and facilitate simultaneously slowing down the Gibbs free-energy barriers of ORR and OER of Li-O₂ batteries. Therefore, we believe that the deliberately-designed cross-scale catalyst accompanied with different scales of catalytic centers is highly desired to meet the ORR/OER catalysis needs for Li-O₂ batteries.

Herein we present a fresh atomic Ru-promoted cross-scale catalyst composed of ultrafine RuPt alloy nanoparticles and surrounding atomically dispersed RuPt pairs on two-dimensional porous carbon (RuPt NPs@RuPt-N-C). The Ru alloying functionalization both on Pt nanocrystal and Pt single atom fundamentally induces the efficient shift of inter-d-orbital electron. This contributes to optimizing electronic structure and tailoring oxygen-involved intermediates adsorption/desorption capability of Pt centers, thereby making RuPt NPs@RuPt-N-C particularly preferred for Li-O₂ batteries. More importantly, according to experimental results and theoretical simulation, a fresh viewpoint on the bifunctional catalysis mechanism in Li-O₂ batteries is first demonstrated for this cross-scale catalyst with different coordination geometries. For Pt NPs@Pt-N-C without Ru functionalization, only Pt-N-C works as ORR/OER active centers, deteriorating the utilization efficiency of Pt NPs. While for RuPt NPs@RuPt-N-C, during ORR, the electron activation effect from atomic Ru, the Pt NPs center is prior to manipulating the nucleation and growth of the hierarchical nanoflower Li₂O₂. When coming to the following OER, the adjacent RuPt atom pairs with superior O₂ desorption characteristic work as an active center can further catalyze the rapid decomposition of Li₂O₂. Hence the potential ORR/OER active centers are fundamentally altered via Ru promotion and the sequential catalysis centers with dual-type ensemble effects

contribute to minimizing both the ORR and OER RDS energy barrier, thus distinctly decreasing the redox overpotential. Impressively, the RuPt NPs@RuPt-N-C cathode exhibits an ultralow overpotential of 0.43 V under a cut-off capacity of 1000 mA g⁻¹. Its polarization can much reduce to 0.66 V even under deep discharge-charge process, among the best in the reported carbon-supported catalysts. Furthermore, RuPt NPs@RuPt-N-C harvests superior cycle life of 209 and 176 cycles at large current densities of 200 and 500 mA g⁻¹, respectively. We believe this finding opens an avenue toward designing efficient catalysts at the atomic level for high-performance Li-O₂ batteries and beyond.

2. Experimental section

2.1. Materials preparation

Typically, 1 g chloroplatinic acid hexahydrate and 0.1 g urea were grounded in mortar for an hour. Then the mixture was annealed at 750 °C in a tube furnace with a heating rate of 4 °C min⁻¹ under argon atmosphere. The obtained product was collected and grounded to black powder. Then the sample was washed twice by ethyl alcohol and deionized water to remove residual sodium carbonate. Later, N-C was synthesized after an overnight dry spell. The as-obtained N-C powder (10 mg), H₂PtCl₆·6 H₂O (14.89 mg) and RuCl₃·xH₂O (1.98 mg) were mixed in 30 ml N,N-Dimethylformamide solution with the Pt/Ru mole ratio as 3:1. Then, the mixed solution was stirred at 60 °C for 8 h. After that, it was centrifuged to gain the sediment and the moist powders were subsequently dried in an oven at 80 °C for a whole night. Finally, the dried powders were heated at 600 °C for 2 h under H₂/Ar with a temperature ramp rate of 5 °C min⁻¹, yielding RuPt NPs@RuPt-N-C dark powders (10 mg). Pt NPs@Pt-N-C was obtained without the addition of RuCl₃·xH₂O.

2.2. Materials characterization

The morphologies of the samples were studied on a field emission scanning electron microscope (SEM, Hitachi SU-8010) and transmission electron microscopy (Talos 200 S, FEI). HAADF-STEM characterizations were obtained from a FEI Themis Z scanning transmission electron microscope with double Cs Corrector operated at 300 kV. XRD patterns of samples were conducted on Rigaku MiniFlex-600 with Cu-K α radiation. Raman spectra were collected using an In Via Reflex Raman spectroscopy with a laser source of 532 nm. The surface elemental composition was conducted through X-ray photoelectron spectroscopy (XPS, Thermo Fisher Scientific ESLAB 250Xi). Brunauer-Emmett-Teller (BET) specific surface and pore size distribution were measured by Beishide 3 H-2000 PS/PM system by nitrogen adsorption-desorption isotherms. X-ray absorption near-edge structure (XANES) and extended X-ray absorption fine structure (EXAFS) spectra were recorded by the BL14B2 station at SPring-8 of the Japan synchrotron radiation research institute, where a pair of channel-cut Si (111) crystals was employed to achieve a monochromatic X-ray beam. The storage ring was operated under the energy of 8.0 GeV with an average electron current of 99.5 mA. The EXAFS profiles fitting were carried out by virtue of the Athena and Artemis programs of the Demeter data analysis packages which equip with the FEFF6 program. Element contents was determined by ICP-OES measurements conducted on Thermo Fisher iCAP PRO instrument.

2.3. Electrochemical measurements

Before assembled, the catalyst components (80 wt%) was dissolved in 1-methyl-2-pyrrolidone (NMP) after mixing with carbon (10 wt% of Timcal Super C65) and PVDF (10 wt%) onto carbon paper (14 mm). Then, the working cathode was obtained after a 12 h drying time under vacuum condition at 45 °C. The catalysts loading was 0.4–0.5 mg cm⁻². Subsequently, the 2032 coin cells consist of a Li anode, a glass fiber separator (GF/D), cathode catalysts and 180 μL electrolyte (1 M LiTFSI /

TEGDME), were assembled under an argon atmosphere in a glove box. After that, the cells were held in a hermetic box at open circuit for 10 h, filled with dried pure O₂ (99.999%, 1.0 atm). Finally, the electrochemical tests were investigated by a Land battery system. Electrochemical workstation (CHI760e) was employed for the CV tests with the scan rate of 0.1 mV s⁻¹ and voltage from 2.0 to 4.5 V. EIS tests were also conducted in a frequency range of 0.01–10⁵ Hz by the same instrument. All the tests are performed at a room temperature of 25 °C.

2.4. Calculation detail

All theoretical calculations were performed, supported by density functional theory (DFT), as carried out in the Vienna ab initio simulation package (VASP) [30,31]. The generalized gradient approximation in the Perdew-Burke-Ernzerhof functional (GGA-PBE) was used to deal with the electron exchange and correlation energy [32]. The valence orbitals of Li (2 s), O (2 s, 2p), Ru (4d, 5 s), N (2 s, 2p), Pt (6d, 5 s) and C (2 s, 2p) were indexed by plane-wave basis sets under the condition of cutoff energies of 500 eV. The k-point sampling was set conducting the Monkhorst-Pack scheme with a (3 × 3 × 1) mesh for the surface models with and without adsorbates, and a (1 × 1 × 1) mesh for single-molecule adsorbates. The convergence criteria for the electronic self-consistent iteration and force were set to 10⁻⁵ eV and 0.02 eV·Å⁻¹, respectively [33,34].

3. Results and discussion

3.1. Microstructure characterization

As depicted in Fig. 1a, the RuPt NPs@RuPt-N-C catalyst is fabricated through a facile metal ions adsorption and following co-reduction strategy. The N-doped two-dimensional (2D) carbon nanosheets were initially obtained via pyrolysis of sodium citrate and urea [35]. Then, Ru, Pt ions with molar ratio of 1:3 were co-trapped onto the defective N-C matrix. After higher-temperature calcination, partial metal ions were in situ self-assembled into well-crystallized ultrafine RuPt alloy nanocrystals, and additional metal ions that do not participate in crystallization were stabilized as monodispersed RuPt single atoms. Then the RuPt NPs@RuPt-N-C hybrid with dual cross-scale active sites and robust site-support structure was constructed. Furthermore, considering the ORR/OER electrocatalysis of Li-O₂ batteries occurs as interfacial reaction, these active components are adequately exposed as interfacial sites, benefiting maximizing atomic utilization efficiency. To disclose the critical function of Ru atoms, the Pt NPs@Pt-N-C contrast catalyst was also fabricated without Ru precursor.

The scanning electron microscopy (SEM) images in Fig. S1 show the porous nanosheet structure of RuPt NPs@RuPt-N-C is well maintained after loading RuPt species. As shown in high angle annular dark-field scanning transmission electron microscopy (HAADF-STEM) image of RuPt NPs@RuPt-N-C (Fig. 1b), a great deal of RuPt alloy nanoparticles with an average diameter of 6 nm are homogeneously scattering over the surface of the N-rich carbon nanosheets, consistent with the high-resolution transmission electron microscopy (HR-TEM) images (Fig. S2). More importantly, the high magnification HAADF-STEM image in Fig. 1c confirms the lots of atomically dispersed RuPt sites (marked by yellow and dark green circles, respectively) evenly distributed neighboring to RuPt alloy nanoparticles. The Z-contrast induced atom brightness discrepancy together with the corresponding 3D local relative intensity profiles (Fig. S3b) of the dashed squares captured from Fig. S3a further confirm the constitution of the RuPt atomic pairs due to metal-metal electronic interaction. In detail, the calculated distance between the Pt and Ru single atoms in Fig. S4 is approximately confirmed to be 0.45 nm. Furthermore, as shown in Fig. S5, the calculated average distance between RuPt single atoms pairs and RuPt nanoparticles is estimated to be about 2.3 nm. The much close location between RuPt nanoparticles and atomic pairs contributes to a potential

synergistic effect to expedite the bifunctional catalytic kinetics of Li-O₂ batteries. Analogously, as shown in Fig. S6a-b, Pt alloy nanoparticles with adjacent atomically distributed Pt atom can also be clearly discerned coexist across the entire Pt NPs@Pt-N-C contrast sample. At this point, it is mentioned that due to the critical N-C matrix spatial confinement effect, both the RuPt alloy nanoparticle and RuPt pair are in situ uniformly grown on the out-surface of the porous carbon substrate without agglomeration or overgrowth. This well-designed 0D/2D heterostructure plays a pivotal role in fully exposing multiple active sites without burying underneath, maximizing contact with reactants and providing ideal platform for Li₂O₂ accommodation and O₂ release. These advantages are essential for guaranteeing the overall Li-O₂ batteries electrochemical performance.

Then the detailed nanocrystal lattice information in RuPt NPs@RuPt-N-C and Pt NPs@Pt-N-C are visualized in Fig. 1d and Fig. S6c, respectively. Along with the fast Fourier transform (FFT) pattern (Fig. 1d inset), the well-defined lattice spacings of 2.33 Å, 2.33 Å and 1.98 Å are related to the (1_11), (1_11) and (200) facets of face-centered cubic Pt along the [011] zone axis, respectively. By contrast, the corresponding (1_11) and (1_11) facets of Pt NPs@Pt-N-C match the lattice spacings of 2.25 Å and 2.27 Å. Furthermore, the HAADF-STEM and HR-TEM images in different areas in Fig. S7 provide sufficient evidence for the increased lattice spacings of RuPt NPs@RuPt-N-C. They are stretched by ≈2.6–3.5% than those of Pt NPs@Pt-N-C. This obvious lattice expansion is attributed to alloying effect from the well implantation of Ru into the lattice of Pt nanocrystal, which is consistent with the XRD Rietveld refinement parameters discussed later. Then the high-magnification HAADF-STEM image of RuPt NPs@RuPt-N-C (Fig. 1e) shows several distinct atom columns along the [001] zone axis. Due to the distinct Z-contrast between Pt and Ru, it can be inferred that the random distribution of the darker isolated Ru atoms doped within the brighter Pt nanocrystal. In addition, the corresponding simulated diffraction patterns in Fig. S8 perfectly match with the FFT results in Fig. 1e (inset). More explicitly, the 2D (Figs. S9) and 3D intensity profiles (Fig. 1f) as well as the corresponding simulated atomic distribution (Fig. 1g, Fig. S10) by Vienna ab initio Simulation Package (VASP) calculation further uncover that Ru atom definitely occupies the position of Pt atom within the lattice of RuPt alloy nanocrystal during co-reduction process. This inevitably alters the lattice parameters of Pt matrix and introduces lattice strains within nanoalloy. This can be further evidenced by inverse FFT (IFFT) results and geometric phase analysis (GPA) [36–39]. As shown in the IFFT images of RuPt NPs@RuPt-N-C (Fig. S11a, b), severe lattice distortion can be observed. More importantly, as shown in the corresponding GPA images (Fig. S11c), the strain distributions of ϵ_{xx} assigned to the (111) plane indicate the existence of abundant compressive and stretched strain. In sharp contrast, no evident lattice deformation can be found from Pt NPs@Pt-N-C (Fig. S12). Thus, it can be argued that the implantation of Ru provides the possibility of optimizing the coordination environment and electronic structure in the RuPt alloy nanoparticles. The intensity profiles across two separate RuPt nanoparticles (Fig. S13) and Energy-dispersive X-ray spectroscopy spectrum (Fig. S14) confirm the existence of Ru, Pt, N and C. The thus acquired Ru/Pt molar ratio is 3.5/1, consistent with the inductively coupled plasma optical emission spectroscopic results (ICP-OES, Table S1). The mass percent of Ru and Pt species in RuPt NPs@RuPt-N-C is 0.70 wt% and 4.75 wt%, respectively. Then elemental mapping images (Fig. 1h) demonstrate the uniform distribution of various elements, further confirming the successful preparation of RuPt cross-scale electrocatalysts with dual-type heteroatom ensemble effects.

The X-ray diffraction (XRD) patterns (Fig. S15) demonstrate that compared to Pt NPs@ Pt-N-C, the diffraction peaks of RuPt NPs@RuPt-N-C slightly shift to low angle, ascribe to the introduction of Ru atoms leading to the lattice expansion of RuPt alloy [40]. The corresponding Rietveld refinement parameters of two XRD patterns (Fig. S16 and Table S2) quantitatively show that the calculated unit cell volume and lattice constants of RuPt NPs@RuPt-N-C are larger than that of Pt

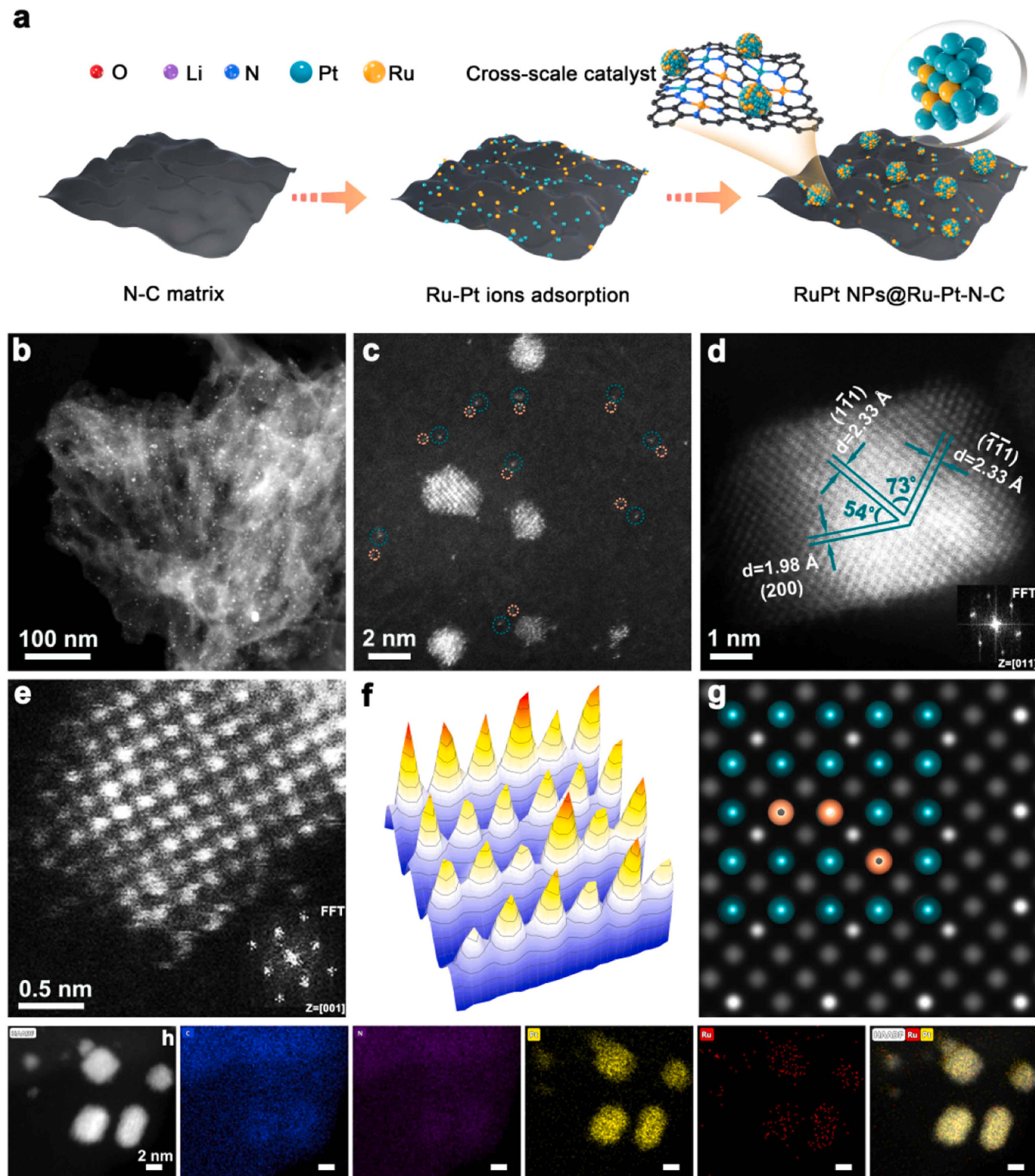


Fig. 1. Electron-microscopy characterizations. (a) Schematic illustration of the synthetic process. (b) HAADF-STEM image of RuPt NPs@RuPt-N-C. (c, d) Zoom-in HAADF-STEM image of RuPt NPs@RuPt-N-C. (e) HAADF-STEM image of the distribution of Ru atoms in Pt nanocrystal. (f) 3D intensity profiles of the RuPt nanocrystal of RuPt NPs@RuPt-N-C in Fig. 1e. (g) The VASP calculated atomic distribution of the RuPt nanocrystal of RuPt NPs@RuPt-N-C in Fig. 1e. The brighter and darker atoms correspond to Ru and Pt atoms, respectively. Schematic atom balls with orange and olive green colors represent Ru and Pt atoms, respectively. (h) Elemental mapping images of C, N, Pt and Ru elements.

NPs@Pt-N-C, faultlessly accordant with the above electron microscope results. The high-solution X-ray photoelectron spectroscopy (XPS) spectrum of N 1 s (Fig. S17) can be distinguished as oxidized N, graphitic, pyrrolic and pyridinic groups. Interestingly, a binding energy negative shift of about 0.1 eV is detected in pyridinic N after loading metal species, indicating there is a tight bonding between pyridinic N and RuPt, constructing robust metal-support electronic interaction and facilitating structural stability during redox cycling. The high-resolution Pt 4 f spectra (Fig. S18a) show the Pt 4 $f_{7/2}$ and Pt 4 $f_{5/2}$ peaks of RuPt NPs@RuPt-N-C are negatively shifted about 0.15 eV in comparison to that of Pt NPs@Pt-N-C, suggesting that due to the higher electronegativity and unfilled d-electron orbitals, Pt inclines to capture electrons from Ru [12,13,41]. Besides, the Ru 3p peaks demonstrate the domination of the oxidation peaks at 463.7 and 485.9 eV in Fig. S18b, implying the major form of Ru $^{\delta+}$ [42–45]. In an attempt to probe the chemical state and more local coordination information, the X-ray absorption fine structure (XAES) results are collected. The X-ray absorption near edge structure (XANES) spectra of Pt L_3 -edge (Fig. 2a) shows the absorption edge position of RuPt NPs@RuPt-N-C is higher than that of Pt NPs@Pt-N-C, while the corresponding white line peak intensity shows a distinct down-shifting tendency, indicating a lower valence state of Pt element in RuPt NPs@RuPt-N-C versus Pt NPs@Pt-N-C. Furthermore, as shown in the Fourier transformed k^3 -weighted extended X-ray absorption

fine structure (FT-EXAFS) spectra in Fig. 2b and Fig. S19, one shell (Pt-N, 1.71 Å) and the other shell (Pt-Pt/Ru, 2.94 Å) are observed for RuPt NPs@RuPt-N-C, respectively. The coordination information of the Pt-N and Pt-Pt/Ru are further confirmed by the fitting results by least squares (Fig. 2c and Table S3). The corresponding first shell Pt-N coordination number of RuPt NPs@RuPt-N-C is estimated as 4.2 at distance of 2.03 Å. And the fitted first shell Pt-Ru and Pt-Pt coordination numbers are estimated as 1.5 and 3.9 at distances of 3.05 Å and 3.11 Å, respectively. Both the two intense characteristic peaks and the fitted coordination information indicate the co-existence of Pt isolated atoms and metal nanoparticles for both RuPt NPs@RuPt-N-C and Pt NPs@Pt-N-C. Meanwhile, after implantation of Ru atoms, the crystal structure of Pt matrix can still be well-maintained due to the appropriate lattice stress mentioned above.

While as shown in the XANES spectra of RuPt NPs@RuPt-N-C at Ru K-edge (Fig. 2d), both the absorption edge and white line intensity are located between the standard RuO₂ and Ru foil, suggesting the cationic valence of Ru. This implies efficient electron migration from Ru 4d to Pt 5d orbital, consistent with the XPS results in Fig. S18a, b. According to the FT-EXAFS and relative fitting profiles of RuPt NPs@RuPt-N-C (Fig. 2e, f), two prominent peaks assigned to Ru-N and Ru-Pt coordination shells are detected at 1.56 Å and 2.66 Å with the absence of typical signals for Ru-Ru scattering path. This further strongly confirms

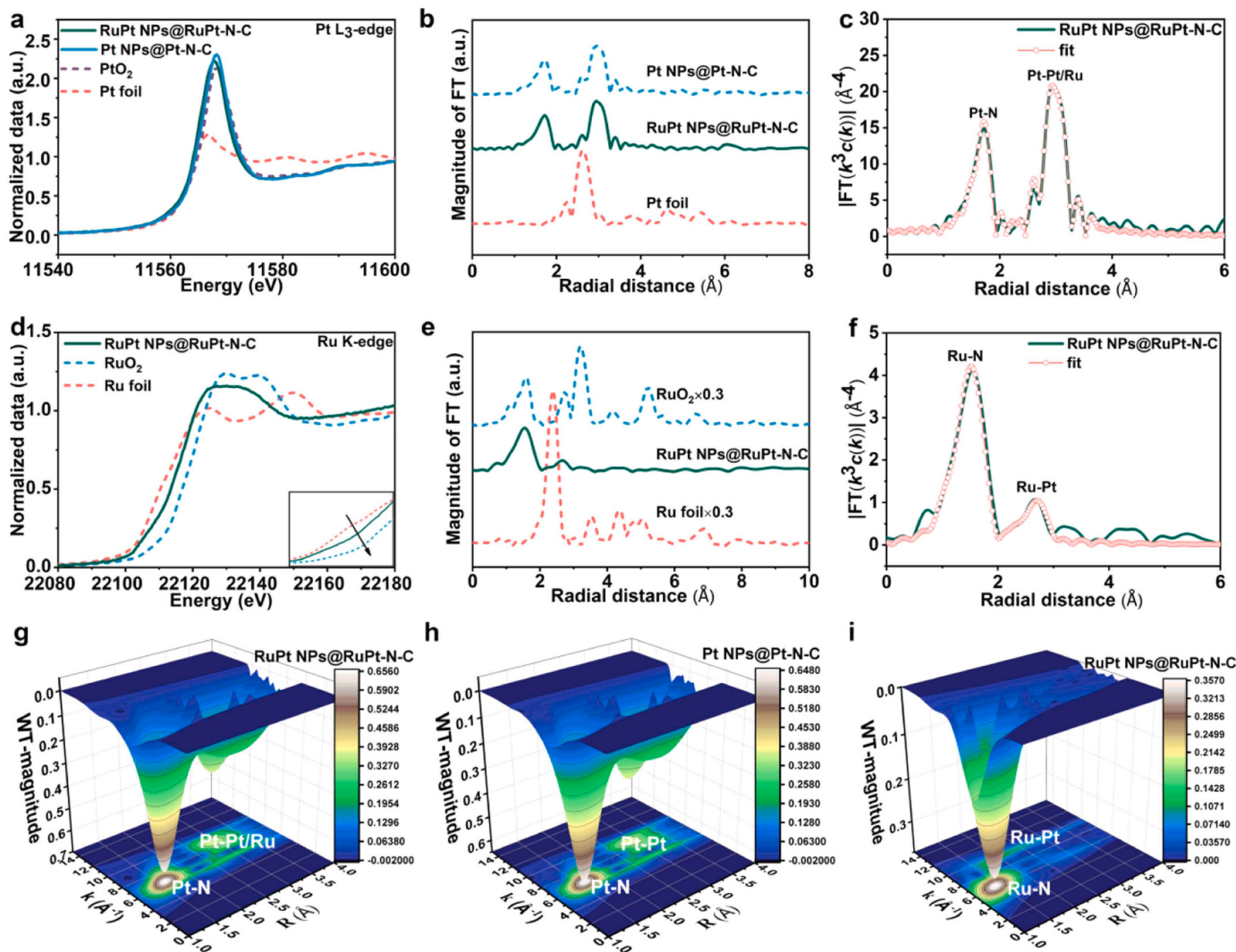


Fig. 2. Structural characterizations of RuPt NPs@RuPt-N-C and Pt NPs@Pt-N-C. (a) XANES spectra of Pt L_3 -edge. (b, c) FT-EXAFS spectra of Pt L_3 -edge and the corresponding fitting curves. (d) XANES spectra of Ru K-edge. (e, f) FT-EXAFS spectra of Ru K-edge and the corresponding fitting curves. (g, h, i) WT-EXAFS analysis of RuPt NPs@RuPt-N-C and Pt NPs@Pt-N-C.

the co-existence of both Ru isolated atoms and doped Ru within alloy matrix in RuPt NPs@RuPt-N-C. The corresponding first shell coordination numbers are estimated as 4.3 and 1.6 at distance of 2.07 Å (Ru-N) and 3.05 Å (Ru-Pt), respectively. In addition, the wavelet transform (WT) images of EXAFS signal summarize coordination geometry both in R and k -space resolution (Fig. 2g-i and Fig. S20). For RuPt NPs@RuPt-N-C, two maximums at 6.5 Å⁻¹ and 8.5 Å⁻¹ (Fig. 2 g) refer to the Pt-N and Pt-Pt/Ru contributions, respectively. Meanwhile, the homologous coordination geometry is observed for Pt NPs@Pt-N-C in Fig. 2 h, further confirming the structure stability after Ru modification. As shown in the Ru K-edge WT contour plots (Fig. 2i), RuPt NPs@RuPt-N-C exhibits that a distinct intensity maximum (6.3 Å⁻¹) and a weak maximum (9.5 Å⁻¹) assigned to Ru-N and Ru-Pt coordination, respectively. As a result, the Ru and Pt species with unsaturated coordinated Pt-N_x, Ru-N_x and Pt-Pt/Ru configurations are integrated within RuPt NPs@RuPt-N-C, which synergistically improve the bifunctional catalytic kinetics of Li-O₂ batteries. Besides, the Raman spectra (Fig. S21) uncover that the introduction of Ru atoms contributes to the improvement of conductivity of RuPt NPs@RuPt-N-C. Moreover, as shown in Fig. S22, RuPt NPs@RuPt-N-C with typical type-IV isotherm characteristics exhibit a notable specific surface area of 370 m² g⁻¹, which is beneficial for three-phase

interfacial reactions for Li-O₂ batteries. To conclude, the microscopy and spectroscopy results demonstrate that the introduction of Ru species regulates the surface electronics of Pt species in RuPt NPs@RuPt-N-C and forms two scales of active centers (RuPt atomic pairs and RuPt alloy nanoparticles, respectively) with different coordination environments. As a frontier of heterogeneous cross-scale catalysts, RuPt NPs@RuPt-N-C is expected to endow flexible manipulation on intermediate evolution and harvest particular catalytic characteristics in comparison to conventional one-fold metal or binary alloy catalysts in Li-O₂ batteries.

3.2. Electrocatalytic performance

Fig. 3a shows the cyclic voltammograms (CV) profiles of the three samples at a scanning speed of 0.1 mV s⁻¹ within 2.0–4.5 V (vs Li⁺/Li). For cathodic sweep, the RuPt NPs@RuPt-N-C and Pt NPs@Pt-N-C catalysts achieve higher ORR onset potential than that of N-C, implying enhanced ORR kinetics. Particularly, RuPt NPs@RuPt-N-C and Pt NPs@Pt-N-C demonstrate two ORR peaks at about 2.70 and 2.35 V, respectively. While, N-C shows only one reduction peak at about 2.5 V. This indicates the loading of Pt active components on N-C has

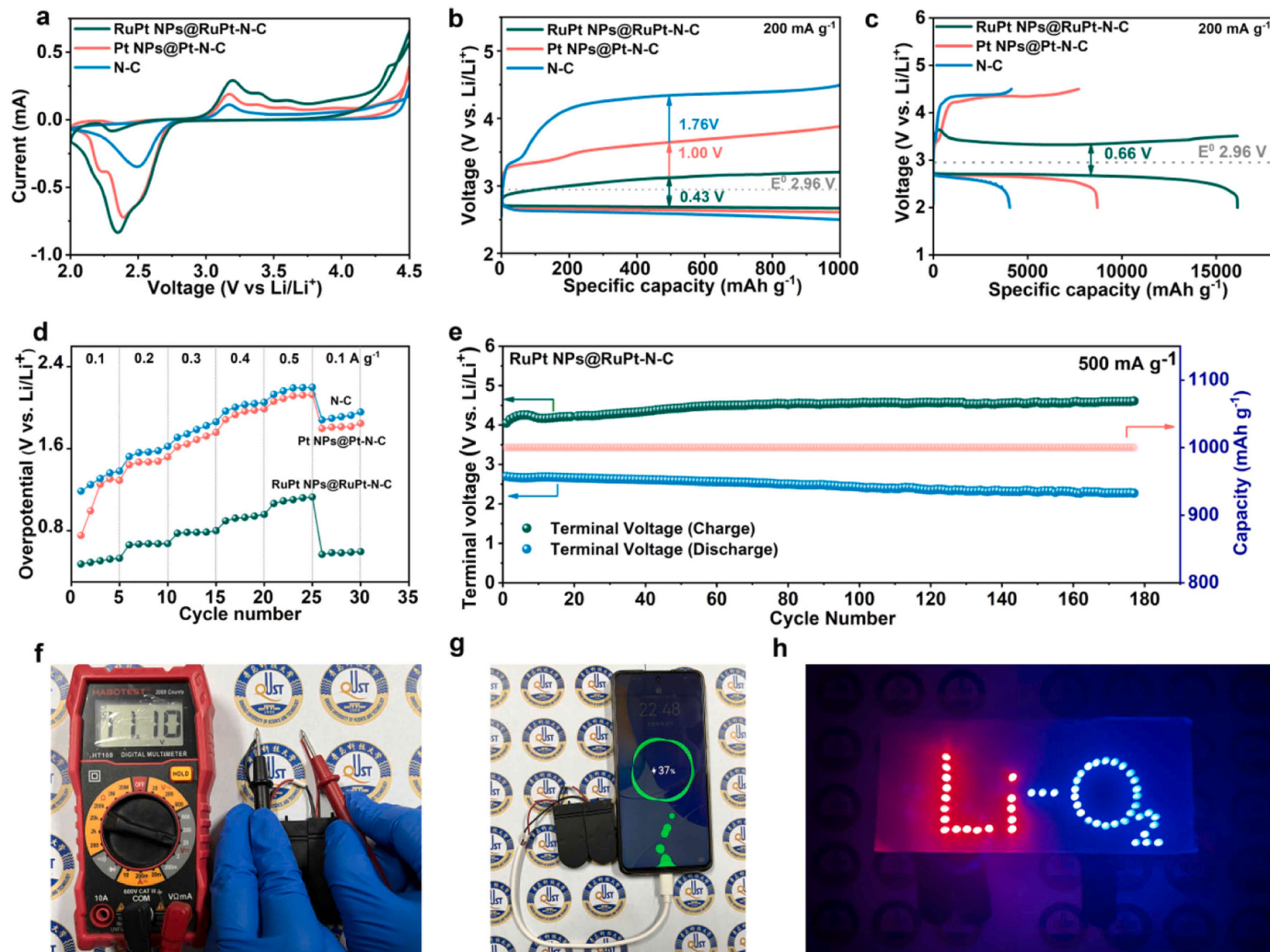


Fig. 3. Electrochemical performance. (a) CV curves of RuPt NPs@RuPt-N-C, Pt NPs@Pt-N-C and N-C electrodes at 0.1 mV s⁻¹. (b) Discharge-charge curves of the three electrodes at a curtailed capacity of 1000 mAh g⁻¹ at 200 mA g⁻¹. (c) The initial deep discharge-charge curves of the three electrodes at 200 mA g⁻¹. (d) Discharge-charge profiles of RuPt NPs@RuPt-N-C electrode at various current densities ranging from 0.1 to 0.5 A g⁻¹ at a cut-off capacity of 1000 mAh g⁻¹. (e) Cycling stability of RuPt NPs@RuPt-N-C electrode at 500 mA g⁻¹ with a limited capacity of 1000 mA h g⁻¹. (f) Photograph of four series-connected batteries with an open-circuit voltage of 11.10 V. (g) Photograph of charging Huawei phone by four cells. (h) Photograph of 50 light-emitting diodes powered by six series-connected batteries.

fundamentally changed the formation path of Li_2O_2 species during ORR, which directly influences the ORR performance as well as the following OER process. Then during anodic sweep, the RuPt NPs@RuPt-N-C and Pt NPs@Pt-N-C catalysts exhibit three distinct oxidation peaks at 3.2, 3.3 and 3.6 V, respectively, indicating the stepwise delithiation and Li_2O_2 decomposition process. This is also absolutely different from that of N-C with only one oxidation peak at 3.2 V. It is mentioned that compared with that of Pt NPs@Pt-N-C and N-C cathodes, the RuPt NPs@RuPt-N-C hybrid exhibits both higher ORR/OER peak current and much enlarged cathodic/anodic peak area [46–49]. This demonstrates that after the further introduction of Ru within Pt nanocrystals and around Pt single atoms, the RuPt NPs@RuPt-N-C catalyst with dual active centers can induce the deposition of more Li_2O_2 product and expedite the reversible oxidation of solid Li_2O_2 , which directly governs the discharge-charge capacity and energy conversion efficiency discussed later. The overall overpotential (Δ) and round-trip efficiency (η) during ORR/OER are generally recognized as critical indicators for evaluating the complex ORR/OER catalytic kinetics of $\text{Li}-\text{O}_2$ batteries [7,49–52]. Then as shown in Fig. 3b, under a restricted capacity of 1000 mAh g^{-1} at 200 mA g^{-1} , the three catalysts demonstrate a similar smooth discharge platform of 2.70 V. However, they demonstrate considerably distinct OER process. Thus the cutoff potential of RuPt NPs@RuPt-N-C is highly suppressed to only 3.21 V, harvesting a much-reduced overpotential of 0.43 V. In sharp contrast, the cutoff potentials of Pt NPs@Pt-N-C and N-C are increased to 3.87 and 4.48 V with Δ of 1.0 V and 1.61 V, respectively. The corresponding η of RuPt NPs@RuPt-N-C is up to 86.2%, outperforming that of Pt NPs@Pt-N-C (74.7%) and N-C (59.9%) counterpart. The summarized Δ_{ORR} and Δ_{OER} in 3D bar graph of Fig. S23 further visually show the unique advantages of RuPt NPs@RuPt-N-C in catalyzing O_2 reduction and evolution kinetics, especially the latter. To experimentally validate the critical roles of the RuPt alloy and RuPt atomic pairs in the ORR and OER process, we have designed the following contrast experiments. The RuPt NPs@N-C was synthesized by prolonging the calcination time to 24 h and the RuPt-N-C counterpart with Ru-Pt single atoms was obtained by the 20 times decrease of the Ru and Pt precursor salts with other synthesis conditions remained unchanged. As shown in Fig. S24, the RuPt NPs@N-C contrast sample exhibits a superior Δ_{ORR} of 0.26 V and an inferior Δ_{OER} of 1.14 V at 200 mA g^{-1} . As shown in Fig. S25, the Δ_{ORR} and Δ_{OER} for the RuPt-N-C contrast sample are 0.44 and 0.63 V at 200 mA g^{-1} , respectively. Above all, by comparing the electrochemistry performance of RuPt NPs@RuPt-N-C, RuPt NPs @N-C and RuPt-N-C, it can be inferred that the RuPt NPs exhibit superior catalytic activity in enhancing ORR process, while RuPt pairs are preferable active sites for OER process. Moreover, when the current density is expanded to 500 mA g^{-1} , RuPt NPs@RuPt-N-C can also achieve competitive overpotentials of 1.0 V (Fig. S26).

Additionally, as shown in Fig. 3c, when deeply discharging and recharging between 2.0 and 4.5 V at 200 mA g^{-1} , RuPt NPs@RuPt-N-C yields initial discharge capacity of 16134 mAh g^{-1} and recharge capacity of 16133 mAh g^{-1} with a coulombic efficiency of 100%, which is much better than that of Pt NPs@Pt-N-C (8707/7707 mAh g^{-1} , 88.5%) and N-C (2159/2205 mAh g^{-1} , 97.9%). Importantly, for RuPt NPs@RuPt-N-C, the charge voltage initially reaches a considerable flat plateau around 3.50 V, affording a small redox voltage gap of 0.66 V. It is mentioned that there is stable interval at ultra-low charging voltage during the whole charge process for RuPt NPs@RuPt-N-C. While for Pt NPs@Pt-N-C and N-C, the charge voltages quickly rise to 4.2 V upon recharging. It can be inferred that the Pt active components play a vital role in enhancing the Li_2O_2 yields and thus improving discharge capacities, but make less contributions to reducing OER overpotential. After the incorporation of Ru, not only the discharge capacity is further increased due to the Ru-Pt alloying interaction, but also the OER polarization is fundamentally reduced. This result affirms that the Ru promotion effect indeed makes RuPt alloy nanocrystals and RuPt atomic pairs work as greatly active ORR/OER electrocatalytic centers in the

RuPt NPs@RuPt-N-C nanostructure, which significantly improves the utilization efficiency and catalytic activity of Pt component. As a crucial criterion for further testing the catalytic activity, rate performance at different current densities (100–500 mA g^{-1}) under a limited capacity of 1000 mAh g^{-1} is investigated. As shown in Fig. 3d and Fig. S27, S28, RuPt NPs@RuPt-N-C exhibits much reduced OER/ORR overpotential among the three samples under all the current densities, and the slight voltage fluctuations are observed during the successive discharge and charge process. Note that, when the current density is reset to initial value, the ORR/OER potentials are well recovered with slight changes for RuPt NPs@RuPt-N-C. These results further indicate the critical role of the Ru promotion effect in apparently enhancing the high-rate catalytic kinetics and reliability. Subsequently, the long-term cycling performances are further investigated. As shown in Fig. S29, the RuPt NPs@RuPt-N-C based $\text{Li}-\text{O}_2$ cell exhibits an extraordinary cycling lifespan of 209 cycles (1045 h) without obvious terminal voltage deterioration with a cutoff capacity of 500 mAh g^{-1} at 200 mA g^{-1} , indicating the long period maintained ORR/OER catalytic kinetics. In sharp contrast, the Pt NPs@Pt-N-C and N-C cathodes can only maintain 164 and 132 cycles with much larger overpotential, respectively (Fig. S30a, S31a). Moreover, when the cutoff capacity and current density are increased as 1000 mAh g^{-1} and 500 mA g^{-1} , RuPt NPs@RuPt-N-C can still maintain 176 cycles (704 h) before the terminal potential decreases to 2.0 V, disclosing its outstanding high rate cycling stability (Fig. 3e, Fig. S32). Nevertheless, the other two cathodes merely remain for 139 and 91 cycles, probably attributed to their unsatisfying catalytic activities (Fig. S30c, S31c). Furthermore, as shown in Tab. S4, the performance comparisons of the RuPt NPs@RuPt-N-C catalyst with those reported noble-metal-containing catalysts unambiguously demonstrate its significant advantage in accelerating $\text{Li}-\text{O}_2$ batteries kinetics. At this point, it can be concluded that the Ru-functionalized cross-scale dual active sites simultaneously make the formation/decomposition of Li_2O_2 species during cycling more feasible with a lower energy barrier, thus affording superior ORR/OER catalytic activity, rate capability and long-term cycling stability.

What's more, to explore the practical application potential, the RuPt NPs@RuPt-N-C based Li-air button cells are assembled. As displayed in Fig. 3 f and g, four RuPt NPs@RuPt-N-C based Li-air button batteries in series realize a superior open-circuit voltage of up to 11.1 V and can successfully charge for a Huawei mobile phone in ambient air, implying its inherent high energy density. Moreover, a $\text{Li}-\text{O}_2$ character pattern consisting of 50 light-emitting diodes is handmade. Then driving with only six button batteries, it can sustain the brightness for more than 70 minutes without the tendency to darken (Fig. 3 h, Fig. S33 and Fig. S34, more details are given in the attached video S1), further illustrating the excellent durability of the well-defined RuPt NPs@RuPt-N-C with cross-scale active sites as superior candidate for practical Li-air batteries.

Supplementary material related to this article can be found online at doi:10.1016/j.apcatb.2024.124203.

3.3. Microstructure evolution of electrodes after ORR/OER

Generally, the nucleation and growth behavior of Li_2O_2 species during ORR induced by cathode catalysts directly decide the discharge performance of $\text{Li}-\text{O}_2$ batteries. And there are two factors that govern the consequent recharge kinetics. The first factor is the morphology, dimension, distribution and crystallization characteristic of the as-formed Li_2O_2 [53]. The second one is the intrinsic OER catalytic efficiency of adjacent catalysts. Herein, to disclose the underlying reaction mechanism of Li_2O_2 and electrochemical performance promotion of this cross-scale catalytic cathode, the microstructure evolutions of Li_2O_2 during discharge and charge are then investigated. Fig. 4a, b and Fig. S35–S37 display the *ex-situ* SEM images of the discharged and recharged cathodes at different states. For RuPt NPs@RuPt-N-C, as the discharge process progresses (2000–8000 mAh g^{-1} –full discharge),

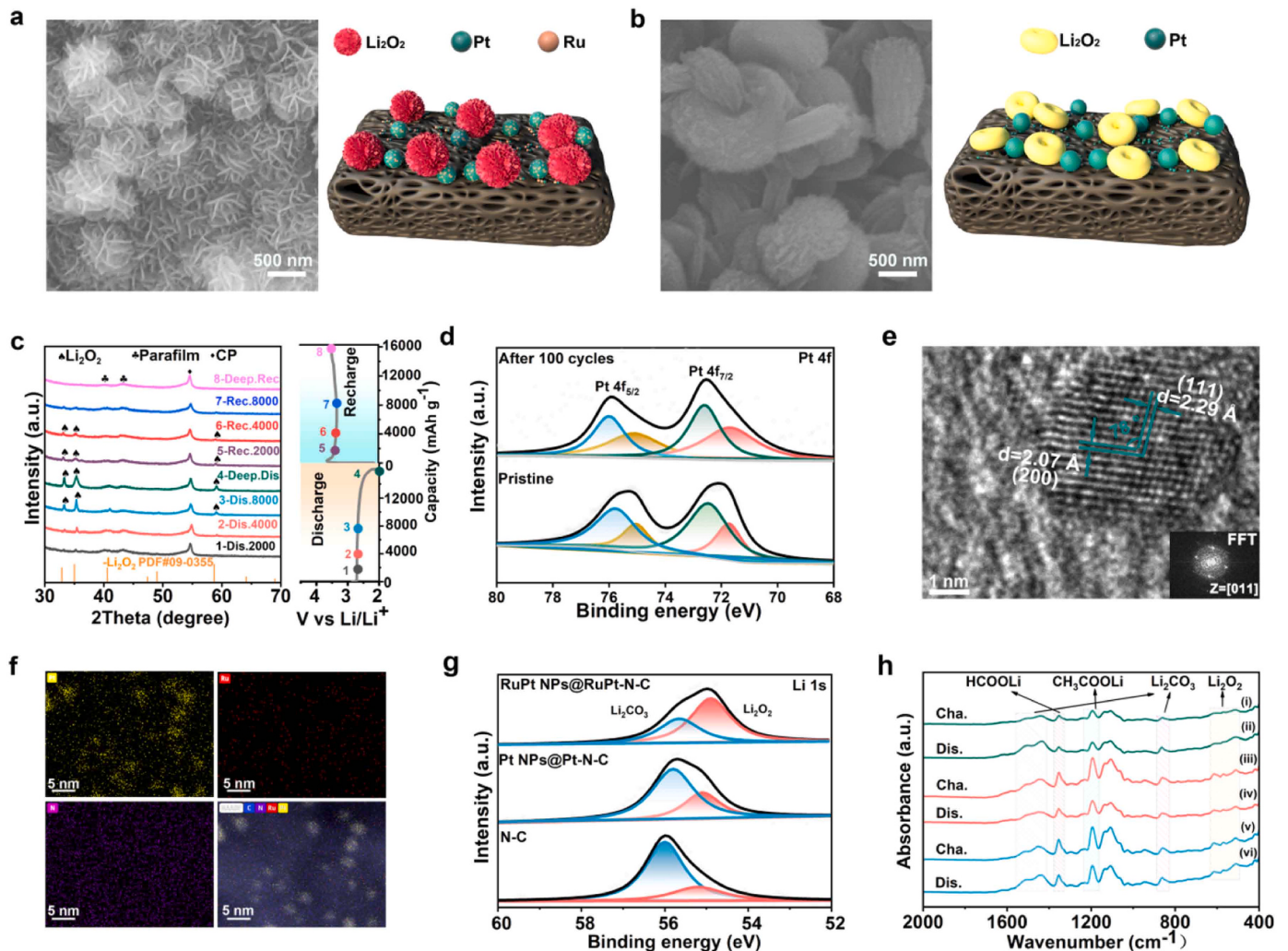


Fig. 4. Ex situ characterizations of discharged and charged electrodes. SEM images and simulated schematic illustration after full discharged for (a) RuPt NPs@RuPt-N-C and (b) Pt NPs@Pt-N-C cathodes. (c) Ex situ XRD patterns of discharged and charged RuPt NPs@RuPt-N-C electrodes during the 1st cycle. (d) Ex situ XPS spectra of pristine, 100th cycled RuPt NPs@RuPt-N-C electrode in Pt 4 f region. (e) Ex situ HRTEM image and (f) elemental mapping images of C, N, Pt and Ru elements of 100th cycled RuPt NPs@RuPt-N-C electrode. (g) Ex situ XPS spectra of 30th three discharged electrodes in Li 1 s region. (h) Ex situ FTIR spectra of the discharged/charged electrodes at the 30th cycle. (RuPt NPs@RuPt-N-C, Pt NPs@Pt-N-C and N-C electrodes are represented by green, red and blue lines, respectively).

cross-linked Li₂O₂ nano-flower assembled by numerous nanosheet units are gradually generated on the catalyst surface, establishing superior catalyst/Li₂O₂/electrolyte three-phase interface. The homogeneously distributed Li₂O₂ species facilitate maximizing utilization efficiency of the potential OER catalysis centers, making the initial Li₂O₂ decomposition at high speed. Moreover this hierarchically breathable Li₂O₂ nano-flower can provide more smooth channels for the following O₂ release [54]. Therefore, the reversible decomposition of solid Li₂O₂ can thoroughly proceed until the full recovery of active surface, which can be evidenced by the SEM images of various charging stages (2000→8000 mAh g⁻¹→full recharge). These advantages jointly contribute to the much-enhanced OER catalytic kinetics and depressed OER overpotential of RuPt NPs@RuPt-N-C. When it comes to Pt NPs@Pt-N-C, without the participation of Ru component, large-sized toroid-shape Li₂O₂ species with an average diameter of about 2.5 μm discretely deposit after full discharge, which is typical in Li-O₂ batteries [55–57]. Similar Li₂O₂ toroids can also be generated for N-C, but with smaller dimension of 1.0 μm. Due to larger mass transfer resistance and inferior interface contact, these bulk Li₂O₂ aggregates are highly energy-consuming to be decomposed. These results can well explain why the Pt NPs@Pt-N-C catalyst achieves increased discharge capacity but fails to ameliorate OER polarization. It can be inferred that due to optimized electronic

structure and adsorption strength on oxygen-involved intermediates from the Ru promotion effect, RuPt alloy nanoparticles and RuPt atomic pairs in RuPt NPs@RuPt-N-C have fully altered the ORR/OER reaction route, which are the critical reasons for the enhancement of Li-O₂ batteries electrochemical performance.

Meanwhile, as shown in the *ex-situ* XRD results at different stages during the first cycle (Fig. 4c and Fig. S38), for all three samples, as ORR progresses (2000→4000→8000 mAh g⁻¹→full discharge), three diffraction peaks at 33.2°, 35.4°, and 59.1° gradually get stronger. They are typical characteristic signals of Li₂O₂ products with the absence of Li₂CO₃ byproduct [3,50,58]. Then once OER, the Li₂O₂ peak strength rapidly declined until thoroughly vanished at full recharge. This indicates the reversible formation and decomposition of Li₂O₂ govern the Li-O₂ batteries electrochemistry in this work. However, for RuPt NPs@RuPt-N-C, the prominent Li₂O₂ peak with more enhanced intensity at various states is distinctly noticed than that of Pt NPs@Pt-N-C and N-C, implying a higher production or better crystallinity of Li₂O₂. According to previous reports, in comparison to amorphous Li₂O₂ with abundant defects and better electron conductivity, the well-crystallized Li₂O₂ species are commonly difficult to decompose [10,59]. Interestingly, as indicated by electrochemical impedance spectroscopy (EIS) in Fig. S39, the much smaller charge transfer resistance of the discharged

RuPt NPs@RuPt-N-C cathode implies that the well-defined hierarchical Li_2O_2 together with close interface contact considerably relieve the passivation effect from insulating Li_2O_2 . This strongly supports the critical role of Ru active constituents in tuning the nucleation/growth behavior of Li_2O_2 . Then after OER, the charge transfer resistance of RuPt NPs@RuPt-N-C demonstrates the best recovery tendency, indicating its superior catalytic activity towards Li_2O_2 decomposition. Herein, thanks to the unique dual active centers configuration of RuPt alloy nanoparticles coupling with RuPt atomic pairs, there realizes a highly desired balance between ORR discharge capacity and OER polarization.

Then the catalyst stability and byproduct accumulation after long period of cycling are evaluated. As depicted in Fig. 4d, as compared with the fresh one, the Pt 4 f spectrum of the 100th cycled RuPt NPs@RuPt-N-C shifts towards higher binding energy. This manifests slight in-situ surface oxidation of Pt metal induced by the continuous exposure within the strong oxidized electrolyte environment, which is crucially important for the enhanced long-term cycling performance of the RuPt NPs@RuPt-N-C catalyst. Weak peaks are detected in the Ru 3p spectra due to its low mass content in the cycled working electrode (Fig. S40). Simultaneously, as shown in the ex-situ HAADF-STEM and EDS images of 100th cycled RuPt NPs@RuPt-N-C (Fig. S41), numerous RuPt nanoparticles (bright spots) are still homogeneously confined on the carbon substrate, indicating superior immunity of RuPt NPs@RuPt-N-C to agglomeration or detachment after repeated cycles. The primary cross-scale catalytic sites embracing RuPt alloy nanoparticle and neighboring RuPt single atom pairs can still be well maintained without aggregation under working conditions in electrolyte environment. The excellent structural stability endows distinguished redox activity and outstanding electrochemical cycling performance. Moreover, as shown in HRTEM image of the 100th cycled RuPt NPs@RuPt-N-C (Fig. 4e), the lattice spacings of 2.07 Å and 2.29 Å are ascribed to (200) and (111) facets of Pt nanocrystal. Additionally, the elemental mapping images in Fig. 4 f verify the uniform distribution of various elements after long-term electrolysis, consistent with that of the fresh catalyst.

Furthermore, the mystery of this durable catalyst is disclosed by the GPA analysis of the (111) and (200) planes in Fig. S42. The strain effects introduced by Ru lattice doping can still be discerned despite long-term enduring the harsh electrolyte environment, which plays a key role in maintaining structural stability and bifunctional catalytic activity of RuPt NPs@RuPt-N-C. The enhanced catalytic efficiency and reduced potential discrepancy can provide an extra bonus of inhibiting parasitic reaction. As shown in the high-resolution Li 1 s spectra for the 30th discharged RuPt NPs@RuPt-N-C (Fig. 4 g), the Li_2O_2 signal at 54.8 eV is dominated while the Li_2CO_3 byproduct at 55.7 eV exhibits a lower ratio. However, for discharged Pt NPs@Pt-N-C and N-C, predominant peaks assigned to Li_2CO_3 are distinctly detected. Then the Fourier transform infrared (FTIR) characterizations offer convicitive evidence of the existence of byproducts of Li_2CO_3 ($860, 1437, 1510 \text{ cm}^{-1}$), CH_3COOLi ($1197, 1615 \text{ cm}^{-1}$) and HCOOLi (1360 cm^{-1}) in the three discharged and recharged electrodes during 10th and 30th cycles in Fig. S43 and Fig. 4 h, respectively [10,12,13]. As expected, trivial byproduct signals are discerned for RuPt NPs@RuPt-N-C electrode, indicating its outstanding anti-passivation capability, which is indispensable for maintaining surface activity and prolonging cycle life. In sharp contrast, insignificant peaks assigned to Li_2CO_3 , HCOOLi , CH_3COOLi are noticed for RuPt NPs@RuPt-N-C and N-C. The gradual accumulations of these byproducts ultimately deteriorate mass transmission pathways and induce battery failure.

3.4. DFT calculations

To further gain insight into the ORR/OER catalytic activity origin of RuPt NPs@RuPt-N-C, in-depth DFT calculations are investigated to disclose the synergistic effect between the cross-scale active sites at atomic scale. Initially, as shown in Fig. S44, four optimized models of RuPt atomic pair, RuPt alloy nanoparticle, Pt single atom and Pt

nanoparticle bound on N-C matrix are established to simulate the potential active sites within RuPt NPs@RuPt-N-C and Pt NPs@Pt-N-C. Generally, in the field of $\text{Li}-\text{O}_2$ batteries, upon discharge, the reactions by one Li^+ , e^- and oxygen molecule first form intermediate LiO_2 as follows: $\text{Li}^+ + e^- + \text{O}_2 \rightarrow \text{LiO}_2$. Then according to binding strength with electrocatalyst surface, LiO_2 species can be evolved into final Li_2O_2 by further electrochemical reaction ($\text{LiO}_2 + e^- + \text{O}_2 \rightarrow \text{Li}_2\text{O}_2$) or chemical disproportionation pathway without extra electron ($\text{LiO}_2 + \text{LiO}_2 \rightarrow \text{Li}_2\text{O}_2 + \text{O}_2$). First, the calculated Gibbs free-energy pathways for the reversible discharge-charge process with possible adsorbates (O_2 , LiO_2 , Li_2O_2 , Li_3O_4 , Li_4O_4) at the different active sites are shown in Fig. 5a-c and Fig. S45, in which the thermodynamic overpotential for the ORR and OER process is represented by $\Delta_{\text{ORR}} = U_{\text{EQ}} - U_{\text{DC}}$ and $\Delta_{\text{OER}} = U_{\text{C}} - U_{\text{EQ}}$ [54,60]. To be specific, U_{EQ} , U_{DC} and U_{C} represent the equilibrium voltage, discharge and charge voltage, respectively. For the four active sites, on the basis of adjacent Gibbs free-energy difference values, the rate-determining step (RDS) for ORR is the reduction of LiO_2 to Li_2O_2 , while the RDS for OER is the oxidation of Li_3O_4 to Li_2O_2 . This further demonstrates single-type active center cannot simultaneously overcome two different energy barriers in $\text{Li}-\text{O}_2$ batteries. It is worth mentioning that in spite of identical RDS, according to quantitative calculation, the Δ_{ORR} values for RuPt alloy nanoparticle, RuPt atomic pair, Pt nanoparticle and Pt single atom are 0.6, 0.8, 1.16 and 0.89 V, respectively. The Δ_{OER} values for the four catalysts are 0.65, 0.51, 1.54 and 1.12 V, respectively. It can be inferred that for Pt NPs@Pt-N-C without Ru functionalization, only Pt-N-C works as preferable ORR/OER active centers, deteriorating the utilization efficiency of Pt nanoparticles. In sharp contrast, due to the Ru promotion effect, not only the Pt nanoparticle is fully activated, which is energetically feasible for expediting ORR process, but also the Pt-N-C is more catalytically active in driving the OER process. Therefore, the ORR/OER active centers are fundamentally changed and a bifunctional catalysis mechanism can be realized in this RuPt NPs@RuPt-N-C cross-scale catalyst during which RuPt alloy nanoparticle and RuPt atomic pair are implemented in sequence as discharge and recharge kinetic promoters, respectively.

To further elucidate deeper reaction mechanism, reactants' adsorption energy and differential charge density are then analyzed. As mentioned above, the $\text{LiO}_2 \rightarrow \text{Li}_2\text{O}_2$ transformation dynamics are the most important factor to be considered for ORR. Thus the adsorption strength of catalysts towards LiO_2 intermediate exerts great influence on the Li_2O_2 growth procedure and then determines ORR electrochemical performance. Fig. S46 display the optimized adsorption construction between various active sites and LiO_2 . Distinctly, Pt nanoparticle and Pt single atom sites have higher adsorption energy for LiO_2 (-4.81 and -5.08 eV). After incorporating Ru, RuPt alloy nanoparticle and RuPt atomic pair exhibit much-reduced adsorption strength for LiO_2 (-4.18 and -4.21 eV). Due to the weaker affinity from RuPt alloy nanoparticle and RuPt atomic pair, more LiO_2 species are not firmly immobilized on the catalyst surface and are inclined to generate Li_2O_2 in disproportionation manner, which induces the continuous self-assembly into nano-flower Li_2O_2 . This can effectively prolong discharge process and reduce ORR polarization.

What's more, to learn the charge distribution on the four active sites and charge transfer between the intermediate LiO_2 and catalysis sites, the corresponding charge density difference and Bader charge analysis are conducted. As shown in Fig. 5d and Fig. S47, compared with RuPt atomic pair (0.10 e^-), RuPt alloy nanoparticle sites are inclined to transfer more electrons (0.52 e^-) to LiO_2 . Therefore RuPt alloy nanoparticle functioned as preferable ORR active site facilitates accelerating the transform process from LiO_2 to Li_2O_2 and enhances the entire ORR kinetics. Although the determined charge transfer number for Pt nanoparticle is larger, its inappropriate binding capability towards LiO_2 limits its ORR performance, which is consistent with the Gibbs free-energy diagrams. When it comes to OER, considering the RDS is the second step of Li_3O_4 to Li_2O_2 , hence the O_2 molecule desorption kinetic governs the whole OER performance (Fig. S48, 49). Specially, RuPt

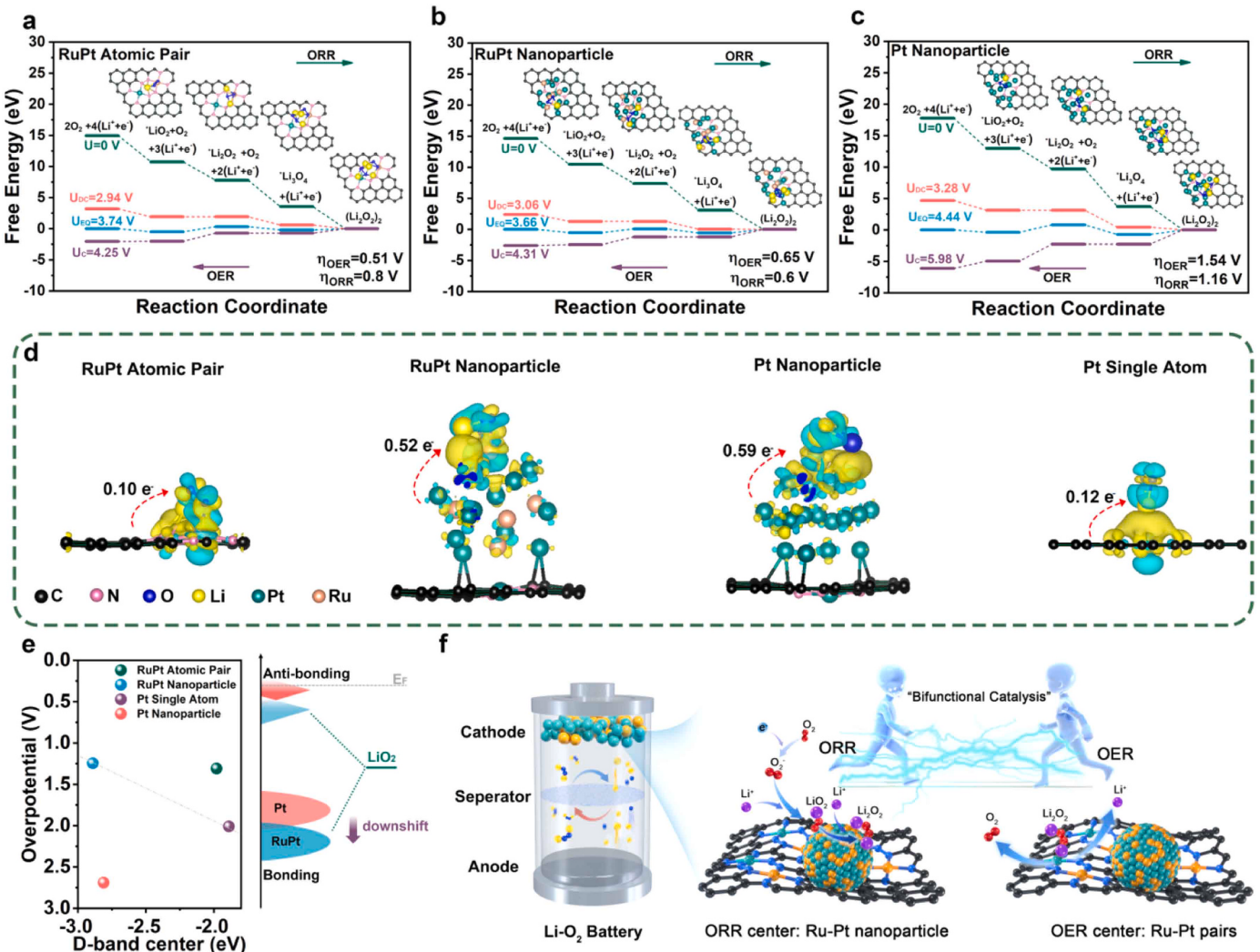


Fig. 5. DFT calculations and proposed mechanisms. Calculated free-energy diagrams for the discharge-charge reactions on the active sites of (a) RuPt atomic pair, (b) RuPt alloy nanoparticle, and (c) Pt nanoparticle. (d) Charge density differences for LiO₂* adsorption states and corresponding charge transfer on RuPt atomic pair, RuPt alloy nanoparticle, Pt nanoparticle, Pt single atom active sites from side view, respectively. (e) Scheme illustration of the bond formation between the adsorbate (LiO₂) valence bands and the d states of RuPt. (f) The reaction mechanism of the cross-scale RuPt NPs@RuPt-N-C hybrid.

atomic pair

site exhibits the ultralow adsorption energy for O₂ (-0.09 eV), which is beneficial for promoting the rapid O₂ releasement. In sharp contrast, much higher O₂ binding energies are shown on RuPt nanoparticle (-1.02 eV), Pt nanoparticle (-1.22 eV) and Pt single atom (-1.72 eV). Hence, the RuPt atomic pair site is supposed to act as an ideal OER active center. Furthermore, Fig. 5e and Fig. S50 display the projected electron density of states (PDOS) of the four active sites. In comparison to that of Pt nanoparticle (-1.99 eV), the d-band center of RuPt alloy nanoparticle is negatively shifted to -2.05 eV. A similar trend also has been demonstrated for RuPt atomic pair (-2.89 eV) and Pt single atom (-2.81 eV). This indicates that due to internal d-d orbital electronic interaction and efficient lattice strain, the d-band position of Pt center is shifted away from Fermi level for RuPt alloy nanoparticle and RuPt atomic pair. This triggers an increase of the occupation of Pt antibonding states, corresponding to suppressed adsorption strength between active site and oxygen-involved reactants, which rationally clarifies the reason why RuPt alloy nanoparticle and RuPt atomic pair configuration exhibit weakened affinity towards LiO₂ and O₂ as mentioned in Fig. S46 and Fig. S48 [12,13,61]. At this point, based on the experiment and simulation data, it is concluded that the simultaneous implantation of Ru atoms into two scale sites induces the optimization of the local

coordination environment and electronic structure of metal centers. As Fig. 5 f depicted, this makes the RuPt alloy nanoparticle and RuPt atomic pair work as preferable ORR and OER sites, respectively. Then, these dual active sites are indispensable to readily drive the reversible ORR and OER processes in a high-efficiency catalysis manner. This finally improves the redox kinetics and electrochemical performances of RuPt NPs@RuPt-N-C based Li-O₂ batteries.

4. Conclusions

In summary, to solve the intrinsic contradiction of active site competition between ORR and OER in Li-O₂ batteries, we propose a fresh Ru promoted bifunctional catalysis strategy within a cross-scale catalyst composed of RuPt alloy nanoparticle and neighboring RuPt single atom pairs. The rational integrated RuPt alloy nanoparticle with RuPt single atom pairs with different coordination environments provide an opportunity to drive ORR and OER in sequence. The experimental and mechanistic analyses unveil that totally different from the Pt-N-C governed onefold ORR/OER active site in Pt NPs@Pt-N-C, the in-situ introduction of Ru within Pt nanocrystal induces distinct electron delocalization, fully activating the catalytic capability of Pt nanocrystal. This contributes to down-shifting d band center of central Pt atoms and

weakening affinity towards LiO_2 intermediate, which fundamentally modify the nucleation and growth behaviors of Li_2O_2 . Hence ORR process can be catalytically expedited through RuPt nanoparticles. For OER process, neighboring RuPt single atom pairs possess preferable O_2 adsorption energy, thereby distinctly accelerating O_2 release and Li_2O_2 decomposition kinetics, which contribute to narrowing OER voltage gap. As expected, the RuPt NPs@RuPt-N-C catalyst with cross-scale catalytic sites maximizes active atom utilization and realizes an efficient balance between discharge capacity and recharge polarization. Then, RuPt NPs@RuPt-N-C based Li-O₂ batteries harvest an ultralow overpotential of 0.43 V and long-lasting cycling life of 209 cycles (1045 h) at 200 mA g⁻¹. This work first verifies the feasibility of cross-scale catalysts with bifunctional catalysis activity in Li-O₂ batteries and provides inspiration for the construction of high-efficiency catalysts in other metal-air batteries.

CRediT authorship contribution statement

Shenlong Zhao: Writing – review & editing, Supervision, Investigation, Funding acquisition, Conceptualization. **Xiaojun Wang:** Writing – review & editing, Formal analysis. **Yu Tian:** Data curation, Conceptualization. **Jingrui Sun:** Methodology, Investigation. **Lei Shi:** Writing – review & editing, Formal analysis. **Shan Guo:** Software, Methodology, Formal analysis. **Yunjie Liu:** Investigation, Formal analysis, Conceptualization. **Peng Wang:** Writing – review & editing, Supervision, Investigation, Funding acquisition, Conceptualization. **Yun Guo:** Writing – original draft, Methodology, Investigation, Formal analysis. **Zhiming Liu:** Writing – review & editing, Supervision, Investigation, Funding acquisition, Conceptualization.

Declaration of Competing Interest

The authors declare no competing financial interest

Data Availability

Data will be made available on request.

Acknowledgements

This work was funded by the National Natural Science Foundation of China (Grant Nos. 21905152, 52302273), the Taishan Scholar Project of Shandong Province of China (Grant Nos. tsqn202211160 and tsqn202312199), the Youth Innovation Team Project for Talent Introduction and Cultivation in Universities of Shandong Province, the Shandong Provincial Natural Science Foundation of China (Grant Nos. ZR2023QE176) and the China Postdoctoral Science Foundation (Grant Nos. 2022M713249).

Appendix A. Supporting information

Supplementary data associated with this article can be found in the online version at [doi:10.1016/j.apcatb.2024.124203](https://doi.org/10.1016/j.apcatb.2024.124203).

References

- [1] W.-J. Kwak, Rosy, D. Sharon, C. Xia, H. Kim, L.R. Johnson, P.G. Bruce, L.F. Nazar, Y.-K. Sun, A.A. Frimer, M. Noked, S.A. Freunberger, D. Aurbach, Lithium–Oxygen batteries and related systems: potential, status, and future, *Chem. Rev.* 120 (2020) 6626–6683, <https://doi.org/10.1021/acs.chemrev. . 9b00609>.
- [2] L. Liu, H. Guo, L. Fu, S. Chou, S. Thiele, Y. Wu, J. Wang, Critical advances in ambient air operation of nonaqueous rechargeable Li-Air batteries, *Small* 17 (2021) e1903854, <https://doi.org/10.1002/smll.201903854>.
- [3] P. Wang, Y. Ren, R. Wang, P. Zhang, M. Ding, C. Li, D. Zhao, Z. Qian, Z. Zhang, L. Zhang, L. Yin, Atomically dispersed cobalt catalyst anchored on nitrogen-doped carbon nanosheets for lithium-oxygen batteries, *Nat. Commun.* 11 (2020) 1576, <https://doi.org/10.1038/s41467-020-15416-4>.
- [4] S.T. Plunkett, A. Kondori, D.Y. Chung, J. Wen, M. Wolfman, S.H. Lapidus, Y. Ren, R. Amine, K. Amine, A.U. Mane, M. Asadi, S. Al-Hallaj, B.P. Chaplin, K.C. Lau, H.-H. Wang, L.A. Curtiss, A new cathode material for a Li–O₂ battery based on lithium superoxide, *ACS Energy Lett.* 7 (2022) 2619–2626, <https://doi.org/10.1038/s41467-020-15416-4>.
- [5] Q. Han, W. Guo, X. He, T. Liu, X. Liu, X. Zhu, T. Bian, L. Jiang, J. Lu, Y. Zhao, Decoupling mass transport and electron transfer by a double-cathode structure of a Li–O₂ battery with high cyclic stability, *Joule* 6 (2022) 381–398, <https://doi.org/10.1016/j.joule.2022.01.003>.
- [6] X. Bi, J. Li, M. Dahbi, J. Alami, K. Amine, J. Lu, Understanding the role of Lithium Iodide in Lithium–Oxygen batteries, *Adv. Mater.* 34 (2021) e202106148, <https://doi.org/10.1002/adma.202106148>.
- [7] Z. Sun, X. Zhao, W. Qiu, B. Sun, F. Bai, J. Liu, T. Zhang, Unlock restricted capacity via O–Ce hybridization for Li–Oxygen Batteries, *Adv. Mater.* 35 (2023) e2210867, <https://doi.org/10.1002/adma.202210867>.
- [8] L.N. Song, W. Zhang, Y. Wang, X. Ge, L.C. Zou, H.F. Wang, X.X. Wang, Q.C. Liu, F. Li, J.J. Xu, Tuning lithium-peroxide formation and decomposition routes with single-atom catalysts for lithium–oxygen batteries, *Nat. Commun.* 11 (2020) 2191, <https://doi.org/10.1038/s41467-020-15712-z>.
- [9] Y. Wu, B. Zhao, X. Zhao, L. Han, Y. Shang, Z. Niu, Y. Liang, X. Zhang, Z. Jiang, F. Li, A. Cao, Compressible, gradient-immersion, regenerable carbon nanotube sponges as high-performance lithium–oxygen battery cathodes, *Mater. Today* 59 (2022) 68–79, <https://doi.org/10.1016/j.mattod.2022.07.005>.
- [10] P. Wang, D. Zhao, X. Hui, Z. Qian, P. Zhang, Y. Ren, Y. Lin, Z. Zhang, L. Yin, Bifunctional catalytic activity guided by rich crystal defects in $\text{Ti}_3\text{C}_2\text{MXene}$ Quantum Dot clusters for Li–O₂ batteries, *Adv. Energy Mater.* 11 (2021) e2003069, <https://doi.org/10.1002/aenm.202003069>.
- [11] J. Zheng, W. Zhang, R. Wang, J. Wang, Y. Zhai, X. Liu, Single-atom Pd-N₄ Catalysis for stable low-overpotential Lithium–Oxygen battery, *Small* 19 (2023) e2204559, <https://doi.org/10.1002/smll.202204559>.
- [12] Y. Zhou, Q. Gu, K. Yin, Y. Li, L. Tao, H. Tan, Y. Yang, S. Guo, Engineering e(g) orbital occupancy of Pt with Au alloying enables reversible Li–O₂ batteries, *Angew. Chem. Int. Ed.* 61 (2022) e202201416, <https://doi.org/10.1002/anie.202201416>.
- [13] Y. Zhou, K. Yin, Q. Gu, L. Tao, Y. Li, H. Tan, J. Zhou, W. Zhang, H. Li, S. Guo, Lewis-Acidic PtIr multipods enable high-performance Li–O₂ batteries, *Angew. Chem. Int. Ed.* 60 (2021) 26592–26598, <https://doi.org/10.1002/anie.202114067>.
- [14] Y. Ding, Y. Huang, Y. Li, T. Zhang, Z.S. Wu, Regulating surface electron structure of PtNi nanoalloy via boron doping for high-current-density Li–O₂ batteries with low overpotential and long-life cyclability, *SmartMat* 5 (2022) e1150, <https://doi.org/10.1002/smml.21150>.
- [15] Z. Tong, C. Lv, Y. Zhou, P.F. Zhang, C.C. Xiang, Z.G. Li, Z. Wang, Z.K. Liu, J.T. Li, S. G. Sun, Highly dispersed Ru–Co nanoparticles interfaced with nitrogen-doped carbon polyhedron for high efficiency reversible Li–O₂ battery, *Small* 18 (2022) e2204836, <https://doi.org/10.1002/smll.202204836>.
- [16] J. Hong, S. Hyun, M. Tsipoka, J.S. Samdani, S. Shanmugam, RuFe alloy nanoparticle-supported mesoporous carbon: efficient bifunctional catalyst for Li–O₂ and Zn–Air Batteries, *ACS Catal.* 12 (2022) 1718–1731, <https://doi.org/10.1021/acscatal.1c04527>.
- [17] X. Hu, G. Luo, Q. Zhao, D. Wu, T. Yang, J. Wen, R. Wang, C. Xu, N. Hu, Ru single atoms on N-doped carbon by spatial confinement and ionic substitution strategies for High-performance Li–O₂ batteries, *J. Am. Chem. Soc.* 142 (2020) 16776–16786, <https://doi.org/10.1021/jacs.0c07317>.
- [18] D. Cao, Y. Hao, Y. Wang, Y. Bai, Y. Li, X. Wang, J. Chen, C. Wu, Platinum nanocrystals embedded in three-dimensional graphene for high-performance Li–O₂ batteries, *ACS Appl. Mater. Interfaces* 14 (2022) 40921–40929, <https://doi.org/10.1021/acsmami.2c10277>.
- [19] Z. Sun, C. Yang, F. Jiang, T. Zhang, Chimerism of carbon by Ruthenium induces gradient catalysis, *Adv. Funct. Mater.* 31 (2021) e2104011, <https://doi.org/10.1002/adfm.202104011>.
- [20] W. Dai, Y. Liu, M. Wang, M. Lin, X. Lian, Y. Luo, J. Yang, W. Chen, Monodispersed Ruthenium nanoparticles on nitrogen-doped reduced graphene oxide for an efficient Lithium–Oxygen battery, *ACS Appl. Mater. Interfaces* 13 (2021) 19915–19926, <https://doi.org/10.1021/acsmami.0c23125>.
- [21] Y. Guo, M. Wang, Q. Zhu, D. Xiao, D. Ma, Ensemble effect for single-atom, small cluster and nanoparticle catalysts, *Nat. Catal.* 5 (2022) 766–776, <https://doi.org/10.1038/s41929-022-00839-7>.
- [22] Y. Li, X. Liu, S. Xue, A. Liu, S. Wen, S. Chen, Boosting the Electrocatalytic performance of CoPt Alloy with enhanced electron transfer via atomically dispersed Cobalt sites, *Small* 19 (2023) e2302170, [https://doi.org/10.1002/smll.202302170.](https://doi.org/10.1002/smll.202302170)
- [23] B. Liu, R. Feng, M. Busch, S. Wang, H. Wu, P. Liu, J. Gu, A. Bahadoran, D. Matsumura, T. Tsuji, D. Zhang, F. Song, Q. Liu, Synergistic hybrid electrocatalysts of Platinum alloy and single-atom Platinum for an efficient and durable oxygen reduction reaction, *ACS Nano* 16 (2022) 14121–14133, <https://doi.org/10.1021/acsnano.2c04077>.
- [24] Q. He, Y. Zhou, H. Shou, X. Wang, P. Zhang, W. Xu, S. Qiao, C. Wu, H. Liu, D. Liu, S. Chen, R. Long, Z. Qi, X. Wu, L. Song, Synergic reaction kinetics over adjacent Ruthenium sites for superb hydrogen generation in Alkaline media, *Adv. Mater.* 34 (2022) e2110604, <https://doi.org/10.1002/adma.202110604>.
- [25] W. Guo, X. Gao, M. Zhu, C. Xu, X. Zhu, X. Zhao, R. Sun, Z. Xue, J. Song, L. Tian, J. Xu, W. Chen, Y. Lin, Y. Li, H. Zhou, Y. Wu, A closely packed $\text{Pt}_{1.5}\text{Ni}_{1-x}\text{Ni–N–C}$ hybrid for relay catalysis towards oxygen reduction, *Energy Environ. Sci.* 16 (2023) 148–156, <https://doi.org/10.1039/d2ee02381d>.
- [26] Y. Zhao, P.V. Kumar, X. Tan, X. Lu, X. Zhu, J. Jiang, J. Pan, S. Xi, H.Y. Yang, Z. Ma, T. Wan, D. Chu, W. Jiang, S.C. Smith, R. Amal, Z. Han, X. Lu, Modulating Pt–O–Pt atomic clusters with isolated cobalt atoms for enhanced hydrogen evolution catalysis, *Nat. Commun.* 13 (2022) 2430, <https://doi.org/10.1038/s41467-022-30155-4>.

- [27] L. Huang, M. Wei, R. Qi, C.L. Dong, D. Dang, C.C. Yang, C. Xia, C. Chen, S. Zaman, F.M. Li, B. You, B.Y. Xia, An integrated platinum-nanocarbon electrocatalyst for efficient oxygen reduction, *Nat. Commun.* 13 (2022) 6703, <https://doi.org/10.1038/s41467-022-34444-w>.
- [28] Y. Zhu, K. Fan, C.S. Hsu, G. Chen, C. Chen, T. Liu, Z. Lin, S. She, L. Li, H. Zhou, Y. Zhu, H.M. Chen, H. Huang, Supported Ruthenium single-atom and clustered catalysts outperform benchmark Pt for Alkaline hydrogen evolution, *Adv. Mater.* 35 (2023) e2301133, <https://doi.org/10.1002/adma.202301133>.
- [29] F. Xiao, Q. Wang, G.-L. Xu, X. Qin, I. Hwang, C.-J. Sun, M. Liu, W. Hua, H.-w Wu, S. Zhu, J.-C. Li, J.-G. Wang, Y. Zhu, D. Wu, Z. Wei, M. Gu, K. Amine, M. Shao, Atomically dispersed Pt and Fe sites and Pt–Fe nanoparticles for durable proton exchange membrane fuel cells, *Nat. Catal.* 5 (2022) 503–512, <https://doi.org/10.1038/s41929-022-00796-1>.
- [30] G. Kresse, J. Furthmüller, Efficiency of ab-initio total energy calculations for metals and semiconductors using a plane-wave basis set, *Comput. Mater. Sci.* 6 (1996) 15–50, [https://doi.org/10.1016/0927-0256\(96\)00008-0](https://doi.org/10.1016/0927-0256(96)00008-0).
- [31] G. Kresse, J. Furthmüller, Efficient iterative schemes for ab initio total-energy calculations using a plane-wave basis set, *Phys. Rev. B* 54 (1996) 11169–11186, <https://doi.org/10.1103/PhysRevB.54.11169>.
- [32] J.P. Perdew, K. Burke, M. Ernzerhof, Generalized gradient approximation made simple, *Phys. Rev. Lett.* 77 (1996) 3865–3868, <https://doi.org/10.1103/PhysRevLett.77.3865>.
- [33] Y. Jiao, Y. Zheng, M. Jaroniec, S.Z. Qiao, Design of electrocatalysts for oxygen- and hydrogen-involving energy conversion reactions, *Chem. Soc. Rev.* 44 (2015) 2060–2086, <https://doi.org/10.1039/C4CS00470A>.
- [34] J.K. Nørskov, J. Rossmeisl, A. Logadottir, L. Lindqvist, J.R. Kitchin, T. Bligaard, H. Jo-P.C.B. Jónsson, Origin of the overpotential for oxygen reduction at a Fuel-Cell cathode, *J. Phys. Chem. B* 108 (2004) 17886–17892, <https://doi.org/10.1021/jp047349j>.
- [35] D. Li, X. Ren, Q. Ai, Q. Sun, L. Zhu, Y. Liu, Z. Liang, R. Peng, P. Si, J. Lou, J. Feng, L. Ci, Facile fabrication of nitrogen-doped porous carbon as superior anode material for Potassium-Ion batteries, *Adv. Energy Mater.* 8 (2018) e1802386, <https://doi.org/10.1002/aenm.201802386>.
- [36] Z. Li, Q. Wang, X. Bai, M. Wang, Z. Yang, Y. Du, G.E. Sterbinsky, D. Wu, Z. Yang, H. Tian, F. Pan, M. Gu, Y. Liu, Z. Feng, Y. Yang, Doping-modulated strain control of bifunctional electrocatalysis for rechargeable zinc-air batteries, *Energy Environ. Sci.* 14 (2021) 5035–5043, <https://doi.org/10.1039/d1ee01271a>.
- [37] S. Liu, Z. Hu, Y. Wu, J. Zhang, Y. Zhang, B. Cui, C. Liu, S. Hu, N. Zhao, X. Han, A. Cao, Y. Chen, Y. Deng, W. Hu, Dislocation-strained IrNi alloy nanoparticles driven by Thermal Shock for the hydrogen evolution reaction, *Adv. Mater.* 32 (2020) e2006034, <https://doi.org/10.1002/adma.202006034>.
- [38] J. Hao, Z. Zhuang, J. Hao, K. Cao, Y. Hu, W. Wu, S. Lu, C. Wang, N. Zhang, D. Wang, M. Du, H. Zhu, Strain Relaxation in metal alloy catalysts steers the product selectivity of electrocatalytic CO₂ reduction, *ACS Nano* 16 (2022) 3251–3263, <https://doi.org/10.1021/acsnano.1c11145>.
- [39] S. Liu, Y. Shen, Y. Zhang, B. Cui, S. Xi, J. Zhang, L. Xu, S. Zhu, Y. Chen, Y. Deng, W. Hu, Extreme environmental thermal shock induced dislocation-rich Pt nanoparticles boosting hydrogen evolution reaction, *Adv. Mater.* 34 (2022) e2106973, <https://doi.org/10.1002/adma.202106973>.
- [40] H. Song, M. Wu, Z. Tang, J.S. Tse, B. Yang, S. Lu, Single Atom Ruthenium-doped CoP/CDs nanosheets via splicing of carbon-dots for Robust Hydrogen Production, *Angew. Chem. Int. Ed.* 60 (2021) 7234–7244, <https://doi.org/10.1002/anie.202017102>.
- [41] D. Chen, G. Zhang, M. Wang, N. Li, Q. Xu, H. Li, J. He, J. Lu, Pt/MnO₂ nanoflowers anchored to boron nitride aerogels for highly efficient enrichment and catalytic oxidation of formaldehyde at room temperature, *Angew. Chem. Int. Ed.* 60 (2021) 6377–6381, <https://doi.org/10.1002/anie.202013667>.
- [42] C. Li, H. Jang, S. Liu, M.G. Kim, L. Hou, X. Liu, J. Cho, P and Mo dual doped Ru ultrasmall nanoclusters embedded in P-Doped porous carbon toward efficient hydrogen evolution reaction, *Adv. Energy Mater.* 12 (2022) e2200029, <https://doi.org/10.1002/aenm.202200029>.
- [43] Y. Sun, Z. Xue, Q. Liu, Y. Jia, Y. Li, K. Liu, Y. Lin, M. Liu, G. Li, C.Y. Su, Modulating electronic structure of metal-organic frameworks by introducing atomically dispersed Ru for efficient hydrogen evolution, *Nat. Commun.* 12 (2021) 1369, <https://doi.org/10.1038/s41467-021-21595-5>.
- [44] Y. Hu, G. Luo, L. Wang, X. Liu, Y. Qu, Y. Zhou, F. Zhou, Z. Li, Y. Li, T. Yao, C. Xiong, B. Yang, Z. Yu, Y. Wu, Single Ru atoms stabilized by hybrid amorphous/crystalline FeCoNi layered double hydroxide for ultraefficient oxygen evolution, *Adv. Energy Mater.* 11 (2020) e202002816, <https://doi.org/10.1002/aenm.202002816>.
- [45] J. Ge, D. Zhang, Y. Qin, T. Dou, M. Jiang, F. Zhang, X. Lei, Dual-metallic single Ru and Ni atoms decoration of MoS₂ for high-efficiency hydrogen production, *Appl. Catal. B: Environ.* 298 (2021) 120557, <https://doi.org/10.1016/j.apcatb.2021.120557>.
- [46] F. Li, M.L. Li, H.F. Wang, X.X. Wang, L.J. Zheng, D.H. Guan, L.M. Chang, J.J. Xu, Y. Wang, Oxygen vacancy-mediated growth of amorphous discharge products toward an ultrawide band light-assisted Li-O₂ batteries, *Adv. Mater.* 34 (2022) e2107826, <https://doi.org/10.1002/adma.202107826>.
- [47] M. Wang, Y. Yao, F. Yang, Z. Tang, J. Ren, C. Zhang, F. Wu, X. Wang, Double spatial confinement on ruthenium nanoparticles inside carbon frameworks as durable catalysts for a quasi-solid-state Li–O₂ battery, *Carbon Energy* 5 (2023) e334, <https://doi.org/10.1002/cey.2334>.
- [48] T. Liu, S. Zhao, Q. Xiong, J. Yu, J. Wang, G. Huang, M. Ni, X. Zhang, Reversible discharge products in Li-Air batteries, *Adv. Mater.* 35 (2023) e2208925, <https://doi.org/10.1002/adma.202208925>.
- [49] X. Cao, C. Wei, X. Zheng, K. Zeng, X. Chen, M.H. Rummeli, P. Strasser, R. Yang, Ru clusters anchored on Magnéli phase Ti₄O₇ nanofibers enables flexible and highly efficient Li-O₂ batteries, *Energy Stor. Mater.* 50 (2022) 355–364, <https://doi.org/10.1016/j.ensm.2022.05.028>.
- [50] X. Zheng, M. Yuan, D. Guo, C. Wen, X. Li, X. Huang, H. Li, G. Sun, Theoretical design and structural modulation of a surface-functionalized Ti₃C₂T_x MXene-based heterojunction electrocatalyst for a Li–Oxygen battery, *ACS Nano* 16 (2022) 4487–4499, <https://doi.org/10.1021/acsnano.1c10890>.
- [51] Y. Wang, S. Pan, Y. Guo, S. Wu, Q.-H. Yang, A bidirectional phase-transfer catalyst for Li-O₂ batteries with high discharge capacity and low charge potential, *Energy Stor. Mater.* 50 (2022) 564–571, <https://doi.org/10.1016/j.ensm.2022.05.037>.
- [52] H. Liang, Z. Gai, F. Chen, S. Jing, W. Kan, B. Zhao, S. Yin, P. Tsikaridas, Fe₃G decorated wood-derived integral N-doped C cathode for rechargeable Li-O₂ batteries, *Appl. Catal. B: Environ.* 324 (2023) 122203, <https://doi.org/10.1016/j.apcatb.2022.122203>.
- [53] H. Yan, W.W. Wang, T.R. Wu, Y. Gu, K.X. Li, D.Y. Wu, M. Zheng, Q. Dong, J. Yan, B.W. Mao, Morphology-Dictated Mechanism of Efficient Reaction Sites for Li₂O₂ Decomposition, *J. Am. Chem. Soc.* 145 (2023) 11959–11968, <https://doi.org/10.1021/jacs.2c12267>.
- [54] X. Han, L. Zhao, J. Wang, Y. Liang, J. Zhang, Delocalized electronic engineering of Ni₅P₄ Nanoroses for durable Li-O₂ Batteries, *Adv. Mater.* 35 (2023) e2301897, <https://doi.org/10.1002/adma.202301897>.
- [55] Z. Sun, X. Lin, W. Dou, Y. Tan, A. Hu, Q. Hou, R. Yuan, M. Zheng, Q. Dong, Redox Mediator with the function of intramolecularly disproportionating superoxide intermediate enabled high-performance Li–O₂ batteries, *Adv. Energy Mater.* 12 (2022) e2102764, <https://doi.org/10.1002/aenm.202102764>.
- [56] Q. Xiong, C. Li, Z. Li, Y. Liang, J. Li, J. Yan, G. Huang, X. Zhang, Hydrogen-bond-assisted solution discharge in aprotic Li–O₂ batteries, *Adv. Mater.* 34 (2022) e210416, <https://doi.org/10.1002/adma.202110416>.
- [57] Y. Zhang, S. Zhang, M. Yuan, Y. Li, R. Liu, C. Nan, C. Chen, Optimal geometrical configuration and oxidation state of cobalt cations in spinel oxides to promote the performance of Li–O₂ battery, *Nano Res* 17 (2023) 221–227, <https://doi.org/10.1007/s12274-023-5526-0>.
- [58] S. Wu, D. Wu, D. Zhang, W. Liu, H. Luo, J. He, Q. Yang, Z. Li, R. Liu, Boosting the activity and stability with dual-metal-N couplings for Li–O₂ battery, *Energy Environ. Mater.* 5 (2021) 918–992, <https://doi.org/10.1002/eam.212210>.
- [59] W. Yu, T. Yoshii, A. Aziz, R. Tang, Z.Z. Pan, K. Inoue, M. Kotani, H. Tanaka, E. Scholtzova, D. Tunega, Y. Nishina, K. Nishioka, S. Nakanishi, Y. Zhou, O. Terasaki, H. Nishihara, Edge-site-free and topological-defect-rich carbon cathode for high-performance Lithium–Oxygen batteries, *Adv. Sci.* 10 (2023) e2300268, <https://doi.org/10.1002/advs.202300268>.
- [60] G. Zhang, G. Li, J. Wang, H. Tong, J. Wang, Y. Du, S. Sun, F. Dang, 2D SnSe Cathode catalyst featuring an efficient facet-dependent selective Li₂O₂ growth/decomposition for Li–Oxygen batteries, *Adv. Energy Mater.* 12 (2022) e2103910, <https://doi.org/10.1002/aenm.202103910>.
- [61] L.-J. Zheng, Y. Yan, X.-X. Wang, L.-N. Song, H.-F. Wang, J.-J. Xu, Regulating electrochemistry kinetics and discharge product selectivity with near-free cobalt single-atom catalyst in Li–O₂ batteries, *Energy Stor. Mater.* 56 (2023) 331–341, <https://doi.org/10.1016/j.ensm.2023.01.024>.